EurJOC
European Journal of Organic Chemistry

Full Papers
doi.org/10.1002/ejoc.202100131

Chemistry Europe
European Chemical Societies Publishing

Special Collection

Room Temperature Phosphorescence from Organic Materials: Unravelling the Emissive Behaviour of Chloro-Substituted Derivatives of Cyclic Triimidazole

Clelia Giannini,*[a] Alessandra Forni,*[b] Daniele Malpicci,[a, b] Elena Lucenti,[b] Daniele Marinotto,[b] Andrea Previtali,[a, b] Lucia Carlucci,[a] and Elena Cariati*[a, b]

Dedicated to Professor Franco Cozzi on the occasion of his 70th birthday.

Purely organic luminophores that exhibit room temperature phosphorescence (RTP) are receiving an ever-growing attention. The design of efficient RTP materials and the understanding of their emissive behaviour, however, remain a challenging task. Herein, to gain further insights into metal-free RTP, we report the synthesis, characterization, and photophysical study of chloro-derivatives of [1,2-*a*:1′,2′-*c*:1″,2″-*e*][1,3,5]triazine or cyclic triimidazole (**TT**). Mono- (**1Cl**), di- (**2Cl**) and tri-chloro-**TT** (**3Cl**) derivatives are prepared by mild chlorination with *N*-chlorosuccinimide (NCS). The three compounds are characterized by aggregation-induced emission (AIE) comprising dual fluorescence and multiple phosphorescences, whose origin is disclosed by crystal structure analysis together with accurate DFT/TDDFT calculations. Comparison with previously reported bromine and iodine **TT** derivatives reveals the new chlorinated compounds as the best performing halogenated AIE members of the family.

Introduction

Compared to the widely used metal containing phosphorescent materials, purely organic compounds showing room temperature phosphorescence (RTP) have attracted attention owing to the benefits they offer, including biocompatibility and low cost. Application of organic RTP in several fields such as bioimaging,[1] anti-counterfeiting,[2] catalysis[3] and displays[4] has been assessed. Many strategies spanning from π-π stacking interactions,[5–7] host-guest systems,[8] halogen bonding,[9,10] and doping in a polymer matrix[11] have been developed to realize organic RTP materials. In this context, we have reported on the intriguing photophysical behaviour of a very simple, small, nitrogen rich organic molecule, namely triimidazo[1,2-*a*:1′,2′-*c*:1″,2″-*e*][1,3,5]triazine, **TT**,[6] and its Br- and I-derivatives.[7,12,13] **TT** is characterized by aggregation-induced emissive (AIE) behaviour, displaying, in particular, ultralong phosphorescence (RTUP) (up to 1 s) under ambient conditions associated with the presence of strong π-π stacking interactions in the crystalline structure.[5] The presence of one or multiple heavy (Br and I) atoms greatly modifies both molecular and solid state photophysical behaviour of the **TT**-scaffold. In particular, in the solid state, a complex excitation dependent photoluminescence with emissions comprising dual fluorescence and multiple phosphorescences, covering a wide portion of the visible region, is observed.[7,12,13] The dual fluorescence has been ascribed to the large energy S_m–S_1 splitting and the low or zero oscillator strength of S_0–S_1 transition, while the multiple phosphorescences have been attributed to both molecular and supramolecular effects. Moreover, all halogenated derivatives display at 77 K, when exciting at high energy (wavelength below 280 nm), a very intense and broad molecular phosphorescence centered at about 580 nm which derives from the presence of $^3(\sigma,\sigma^*)$ and $^3(\sigma,\pi^*)$ T_n levels. These states guarantee an efficient intersystem crossing, ISC (by both El Sayed and heavy atom effects) from the closest S_n levels of $^1(\pi,\pi^*)$ character. The heavy iodine atom effect manifests in originating such emission also at room temperature. At supramolecular level, halogen atom based intermolecular interactions and π-π stacking interactions have been deemed responsible for a broad long-lived component and a structured low-energy RTUP, respectively.

Here we report on the synthesis, characterization and photophysical behaviour of mono-, di- and tri-chloro derivatives of cyclic triimidazole (see Scheme 1), namely 3-chlorotriimidazo[1,2-*a*:1′,2′-*c*:1″,2″-*e*][1,3,5]triazine, 3,7-dichlorotriimidazo[1,2-

---

[a] Dr. C. Giannini, Dr. D. Malpicci, Dr. A. Previtali, Prof. L. Carlucci, Prof. E. Cariati
Dept. of Chemistry
Università degli Studi di Milano and INSTM RU
Via Golgi 19, 20133 Milano, Italy
E-mail: clelia.giannini@unimi.it
elena.cariati@unimi.it
https://www.unimi.it/it/ugov/person/clelia-giannini
https://www.unimi.it/it/ugov/person/elena-cariati

[b] Dr. A. Forni, Dr. D. Malpicci, Dr. E. Lucenti, Dr. D. Marinotto, Dr. A. Previtali, Prof. E. Cariati
Institute of Sciences and Chemical Technologies "Giulio Natta" (SCITEC) of CNR
via Golgi 19, 20133 Milano, Italy
E-mail: alessandra.forni@scitec.cnr.it
http://www.scitec.cnr.it/personale/golgi-ita/alessandra-forni

Supporting information for this article is available on the WWW under https://doi.org/10.1002/ejoc.202100131

Part of the "Franco Cozzi's 70th Birthday" Special Collection.

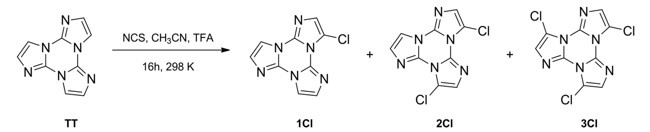

Scheme 1. Synthesis of chloro-TT derivatives.

a:1′,2′-*c*:1″,2″-*e*][1,3,5]triazine and 3,7,11-trichlorotriimidazo[1,2-*a*:1′,2′-*c*:1″,2″-*e*][1,3,5]triazine, hereafter **1Cl**, **2Cl** and **3Cl**, respectively. The obtained results provide evidence that this study is not a mere extension of previous work done on halo-**TT** compounds, but it gives new insight in the photophysics of organic RTP. Moreover, **1Cl**, **2Cl** and **3Cl** reveal as the best performing among the full series, preserving the solid state multifaceted emissive behaviour but with enhanced AIE features (highest quantum yield) with respect to the bromine and iodine analogues.

Results and Discussion

The three new compounds **1Cl**, **2Cl** and **3Cl** were prepared by mild chlorination of **TT** with *N*-chlorosuccinimide (NCS). The derivatives were isolated and purified by standard chromatographic techniques, crystallized for single crystal XRD analyses and characterized by NMR and mass spectrometry. The chlorination with NCS is not specific and provides a mixture of the three compounds **1Cl**, **2Cl** and **3Cl**, according to mass spectrometry data. In our previous work,[7,12,13] we reported the bromination and the iodination of **TT** with *N*-bromosuccinimide (NBS) and *N*-Iodosuccinimide (NIS) respectively, using ACN as solvent and TFA as catalyst. In the latter case we observed a low selectivity towards the mono-derivative, which is a well-known drawback of electrophilic halogenation of aromatic systems. In order to assess the best conditions for obtaining **1Cl**, we report a screening of the electrophilic chlorination of **TT** with NCS in different conditions, to evaluate relevant reaction parameters such as catalyst, solvent and NCS stoichiometry (see Table S1 in the Supporting Information). The optimization of the reaction parameters led to the conclusion that the combination of TFA as catalyst and ACN as solvent seems to be superior to others.

In order to increase **TT** conversion, an increment in the NCS equivalents was also tested, showing a higher conversion and good selectivity in **1Cl** when using 2 equivalents of NCS and increased conversion towards **2Cl** and **3Cl** with higher amounts of NCS.

With optimized conditions in place, the reaction was scaled up; the chlorinating agent was dissolved in ACN and added dropwise to a solution of **TT**, after that the reaction mixture was stirred at RT for 16 hours (see Scheme 1).

Chlorination of **TT** using 2 equivalents of NCS provided **1Cl** and **2Cl** that were isolated as a mixture and purified by silica-gel column chromatography (**1Cl** 47 % yield, **2Cl** 38 % yield). Otherwise, the chlorination using 4 equivalents of NCS allowed to get a mixture of all three halogenated species which were purified by column chromatography (**1Cl** 21 %, yield, **2Cl** 61 % yield, **3Cl** 16 % yield). In both cases the reaction mixture was stirred at RT for 16 hours. Further, the purity was improved by repeated crystallizations from CH$_3$CN for **1Cl** and **2Cl** and from CH$_2$Cl$_2$ (DCM)/MeOH for **3Cl**. This latter solvent mixture also provided crystals suitable for single crystal X-ray diffraction analysis. Furthermore, the structures of **1Cl**, **2Cl** and **3Cl** were elucidated by extensive spectroscopic methods including 1D (^{1}H and ^{13}C) and 2D nuclear magnetic resonance (NMR) experiments as well as mass spectrometry analysis.

1Cl, **2Cl** and **3Cl** crystallize in the P-1, C2/c and P2$_1$/c space groups, respectively, with two molecules, labelled as A and B (in **1Cl** and **3Cl**) and one molecule (in **2Cl**) in the asymmetric unit (see Table S2, Figure S10 for atoms numbering and Figure S11 for different views of crystal packing). The crystal structures of the three compounds share, with that of **TT** itself, the formation of slightly corrugated planes where molecules, in **1Cl** and **2Cl**, are connected through several relatively short C–H···N and C–H···Cl hydrogen bonds, HB ($r_{H\cdots N}$ in the range 2.44–2.65 and 2.46–2.48 Å; $r_{H\cdots Cl}$ equal to 2.92, 2.95 and 2.84, 2.85 Å in **1Cl** and **2Cl**, respectively). On the other hand, the layers of **3Cl** consist of ribbons of A-type molecules, connected through short C–H···N ($r_{H\cdots N} = 2.35$ Å) HB, alternating with B-type molecules, interacting through very short Cl···N ($r_{Cl\cdots N} = 3.014(2)$ Å) halogen bond (XB) together with C–H···N ($r_{H\cdots N} = 2.50$ Å) HB. Additional XB ($r_{Cl\cdots N} = 3.151(2)$ Å) and HB ($r_{H\cdots N} = 2.41$ Å) formed every other molecule join the ribbons with each other (see Figure 1).

The presence of such strong XBs, corresponding to 8.7 and 4.5 % shortening with respect to the sum of Cl and N van der Waals radii, is rather unexpected owing to the absence of strong electron-withdrawing groups on the **TT** scaffold and may be explained by the need to accommodate, within the layers, three rather bulky (compared to hydrogen) chlorine atoms.

These H-bonded (in **1Cl** and **2Cl**) and H/X-bonded (in **3Cl**) layers stack in a slipping manner, evidencing the presence of π-π stacking interactions. The distances between least-squares planes through equivalent triazinic atoms measure 3.408 and 3.182 Å for molecules A and B, respectively, in **1Cl**; 3.307 Å in **2Cl**; and 3.356/3.143 Å for A/B molecules in **3Cl**. Notably such

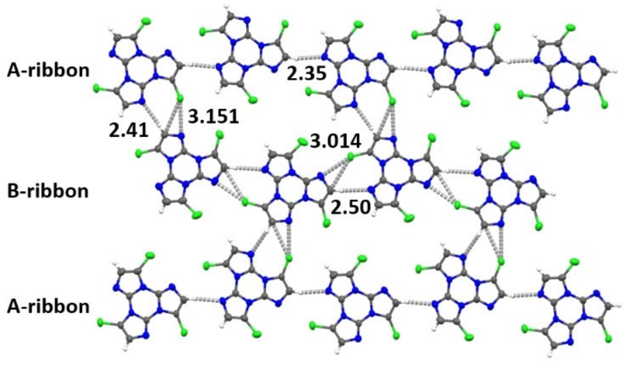

Figure 1. Fragment of **3Cl** crystal packing depicting a layer of A- and B-type molecules. Interatomic contacts (in Å) shorter than the sum of van der Waals radii are shown as grey dashed lines. Ellipsoids at 50 % probability.

layered pattern is disrupted in the analogue **1Br**, **3Br** and **1I** halogenated **TT** derivatives, owing to the presence of strong Br/I···N XBs that dominate over the π-π contribution. In **2Br** and **2I** the two kinds of interaction act in a cooperative way by the formation of planar X_4 XB synthons, conferring high rigidity to the structures. Compared to **TT**, showing almost overlapped molecules with short distances between triazinic centroids (C_{tr}) alternately equal to 3.733 and 3.949 Å, larger slippages are found in the **nCl** structures (see Figure 2). In particular, in **1Cl** each molecule is placed approximately midway two molecules of the adjacent layer with shorter $C_{tr}\cdots C_{tr}$ distances alternately equal to 4.853 and 5.231/5.351 Å. Despite the large molecular slippage, several close intermolecular C···C contacts are present, i.e. C1···C3^{i}, 3.329(5); C2···C13, 3.379(5); C18···C16^{ii}, 3.386(5); C4···C11^{iii}, 3.439(5); C7···C8^{iv}, 3.449(5); C4···C12^{iii}, 3.482(5); C8···C12, 3.486(5) Å, [i = 1-x,y,z; ii = x,-y,-z; iii = 1 + x,y,z; iv = 2-x,1-y,1-z]. Similar relative disposition of the molecules, though with lower slippage, is observed in **2Cl**. Here the $C_{tr}\cdots C_{tr}$ distances are alternately equal to 4.350 and 5.630/5.680 Å and C···C closer contacts are C5···C6^{i}, 3.263(2); C2···C2^{ii}, 3.339(2); C3···C8^{ii}, 3.372(2); C1···C4^{ii}, 3.373(2); C6···C6^{iii}, 3.407(2); C3···C3^{iv}, 3.441(2); C1···C1^{iv}, 3.478(2) Å, [i = 1/2-x,1/2-y,1-z; ii = 1/2-x,1/2-y,2-z; iii = 1-x,y,1.5-z; iv = −x,y,1.5-z]. In **3Cl**, A and B molecules alternate along the stacking axes with $C_{tr}\cdots C_{tr}$ distances alternately equal to 4.486 and 4.621 Å and several C···C and C···N short contacts (C9···C18^{i}, 3.328(3); C2···C11, 3.379(3); C9···C13, 3.456(3); C1···N12^{i}, 3.289(3); C8···N7^{i}, 3.301(3); N2···C10, 3.307(3) Å, i = x-1,y,z). Therefore, looking at the shorter distances between centroids, the slippage increases in the order **TT** ≪ **2Cl** < **3Cl** < **1Cl**.

Photophysical Properties

Diluted solutions of **1**–**3Cl** in DCM (10^{-5} M) display at 298 K absorption bands at wavelength below 300 nm. The three compounds in solution are hardly emissive ($\Phi < 1\%$) with multiple fluorescence and phosphorescence bands (see Figure S12, Figure S27 and Figure S45) to be attributed to aggregated species. This is due to the fact that single molecules of **1**–**3Cl** are substantially non emissive and, the low amount of aggregates present even at concentration as low as 10^{-5} M, dictate the emissive behaviour which resembles that of solid samples (see below). Crystals of **1Cl** are characterized by multiple emissive features (see Figure 3 and Figure S13) with an overall quantum efficiency varying with excitation wavelength ($\Phi < 1\%$ for $\lambda_{exc} = 280$–300 nm; 13 % for $\lambda_{exc} = 310$–340 nm; 24 % for $\lambda_{exc} = 350$–390 nm). In particular, by exciting in the 300–400 nm range, a broad partially resolved band, clearly comprising multiple contributions, is observed in the 320–450 nm interval. By lifetime measurement, it appears that such emission is the result of two fluorescences (one at 333 and 348 nm, HEF, $\tau_{av} = 0.77$ ns; the other, LEF, at about 350 nm, $\tau_{av} = 1.02$ ns, see Figure S15 and Figure S16) and one phosphorescence, HEP (with peaks at 405 and 428 nm, $\tau_{av} = 270$ μs, see Figure S17) which can be resolved from the fast components by excitation at 340 nm. An additional long lived structured emission, MEP, is observed at about 510 nm ($\tau_{av} = 26$ ms, see Figure S18) by exciting at 440 nm.

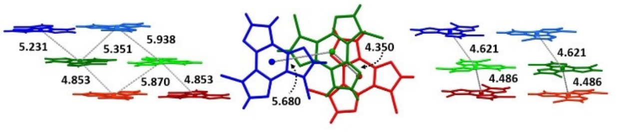

Figure 2. Fragments of crystal packing of **1Cl** (left), **2Cl** (center) and **3Cl** (right) showing three overlapped layers in different colors viewed from side or top (dark/light colors for A/B molecules of **1Cl** and **3Cl**) and distances (in Å) between triazinic centroids.

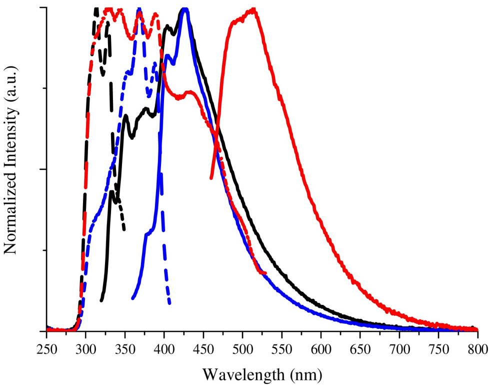

Figure 3. Normalized excitation (dotted lines) and emission (solid lines) spectra of **1Cl** crystals at 298 K. Emission: $\lambda_{exc} = 300$ nm (black), $\lambda_{exc} = 340$ nm (blue) and $\lambda_{exc} = 440$ nm (red). Excitation: $\lambda_{em} = 371$ nm (black), $\lambda_{em} = 427$ nm (blue) and $\lambda_{em} = 550$ nm (red).

At 77 K the same emission bands can be recognized in the spectrum (see Figure 4 and Figure S19) with a better vibronic resolution and longer lifetimes. In particular, by exciting at 300–340 nm a broad band resulting from the overlapping of different vibrationally resolved contributions appears in the spectrum in the 320–480 nm interval. From analysis of the spectrum at different excitations and lifetime measurements, HEF and LEF at 333 and 349 nm ($\tau_{av} = 1.22$ ns, see Figure S21)

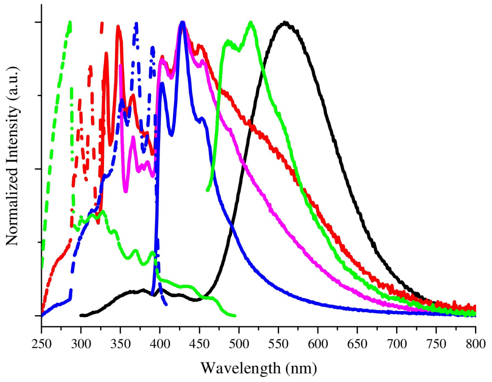

Figure 4. Normalized excitation (dotted lines) and emission (solid lines) spectra of **1Cl** crystals at 77 K. Emission: $\lambda_{exc} = 280$ nm (black), $\lambda_{exc} = 300$ nm (red), $\lambda_{exc} = 327$ nm (magenta), $\lambda_{exc} = 370$ nm (blue) and $\lambda_{exc} = 440$ nm (green). Excitation: $\lambda_{em} = 348$ nm (red), $\lambda_{em} = 428$ nm (blue) and $\lambda_{em} = 515$ nm (green).

and at 367, 378 and 383 nm ($\tau_{av}=4.76$ ns, see Figure S22), respectively, and HEP at 406, 429 and 450 nm ($\tau_{av}=1.66$ ms, see Figure S23) and MEP at 487 and 515 nm ($\tau_{av}=778$ ms, see Figure S24), are recognized. In addition, at 280 nm excitation, an additional broad, unresolved phosphorescence, LEP, at 558 nm ($\tau_{av}=12$ ms, see Figure S25) is activated.

From analysis of excitation spectra (see Figure 3, Figure 4, Figure S14 and Figure S20) different bands can be recognized: one absorption with peaks at 310 and 330 nm ascribable to S_1; a second absorption at 299 nm, visible only at low temperature, to be assigned to a high energy singlet, S_n; an additional lower energy contribution in the 370–390 nm range reasonably produced by molecular triplet levels including T_1 and weak, unresolved, low energy bands in the 400–500 nm interval, probably to be associated with aggregated forms.

Similarly to **1Cl**, crystals of **2Cl** at 298 K, are characterized by a complex, excitation dependent emissive behaviour (see Figure 5 and Figure S28; $\Phi<1\%$ for $\lambda_{exc}=280$–310 nm; 6.3% for $\lambda_{exc}=320$–390 nm; 12% for $\lambda_{exc}=400$–460 nm). In particular, by exciting at 280 nm, a broad emission, LEF, at 397 nm ($\tau_{av}=1.41$ ns, see Figure S30) with a high energy tail, HEF, at 330 nm (with lifetime shorter than the instrumental resolution: 6 ps) and weak signals at 480, 514 and 552 nm fingerprint of MEP are observed. LEF is selectively activated by exciting at 308 nm. Moreover, a broad phosphorescence at 434 nm ($\tau_{av}=1.33$ ms, see Figure S31), HEP, is observed by exciting at 375 nm. Finally, vibrationally resolved long lived MEP component with peaks at 481, 512 and 552 nm ($\tau_{av}=49.13$ ms, see Figure S32), is isolated when exciting at 413 nm. At 77 K, the four emissions are still present (see Figure 6 and Figure S33) together with LEP activated only by exciting at 280 nm. In particular, the following bands are recognized in the spectrum: HEF with vibronic replicas at 329, 339 and 348 nm (lifetime shorter than the instrumental resolution: 6 ps); LEF at 362, 380 and 401 nm ($\tau_{av}=1.48$ ns, see Figure S35); HEP, recognizable through a peak at 436 ($\tau_{av}=4.38$ ms, see Figure S36); MEP at 483, 515 and 554 nm ($\tau_{av}=530$ ms, see Figure S37) and LEP at 549 nm ($\tau_{av}=13$ ms, see Figure S38).

Analysis of excitation spectra (see Figure 5, Figure 6, Figure S29 and Figure S34) reveals the presence of one absorption at about 320 nm, better vibrationally resolved at 77 K (replicas at 310, 320 and 325 nm) ascribable to S_1; a second absorption at 297 nm to be assigned to a high energy singlet, S_n; an additional lower energy contribution at 375 and 398 nm, associated with molecular triplet levels including T_1 and a low energy vibrationally resolved band with peaks at 440 and 469 nm. This latter, is to be assigned to the organization of the dye in tightly bounded π-π aggregates in its crystal structure. In agreement, such low energy contribution appears as a weak and broad band in the excitation spectra of **1Cl**, where looser aggregates are formed. To better support this observation, we prepared and fully photophysically characterized amorphous thin films of **2Cl**, prepared by melting and rapid cooling its powder on a quartz substrate. As for the crystalline phase, the film displays excitation dependent behaviour (see Figure 7 and Figure S39; $\Phi=1\%$ for $\lambda_{exc}=280$–310 nm; 3% for $\lambda_{exc}=320$–370 nm; 6% for $\lambda_{exc}=380$–410 nm). By excitation at 308 nm, an intense emission with peaks at 414 and 434 nm and much weaker high energy replicas at 331, 349 and 366, 382 nm, appear in the spectrum. From lifetime measurements, the high

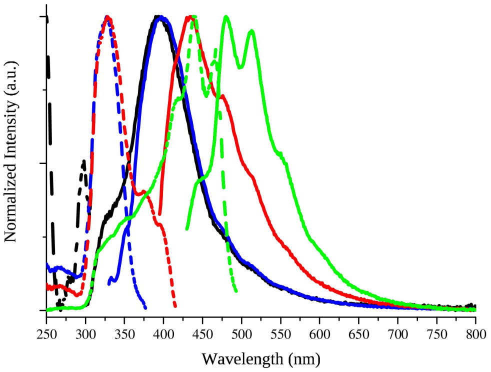

Figure 5. Normalized excitation (dotted lines) and emission (solid lines) spectra of **2Cl** crystals at 298 K. Emission: $\lambda_{exc}=280$ nm (black), $\lambda_{exc}=308$ nm (blue), $\lambda_{exc}=375$ nm (red) and $\lambda_{exc}=413$ nm (green). Excitation: $\lambda_{em}=328$ nm (black), $\lambda_{em}=398$ nm (blue), $\lambda_{em}=436$ nm (red) and $\lambda_{em}=514$ nm (green).

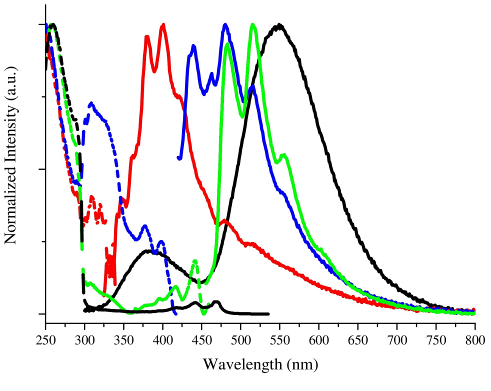

Figure 6. Normalized excitation (dotted lines) and emission (solid lines) spectra of **2Cl** crystals at 77 K. Emission: $\lambda_{exc}=280$ nm (black), $\lambda_{exc}=308$ nm (red), $\lambda_{exc}=400$ nm (blue) and $\lambda_{exc}=434$ nm (green). Excitation: $\lambda_{em}=360$ nm (red), $\lambda_{em}=437$ nm (blue), $\lambda_{em}=481$ nm (green) and $\lambda_{em}=556$ nm (black).

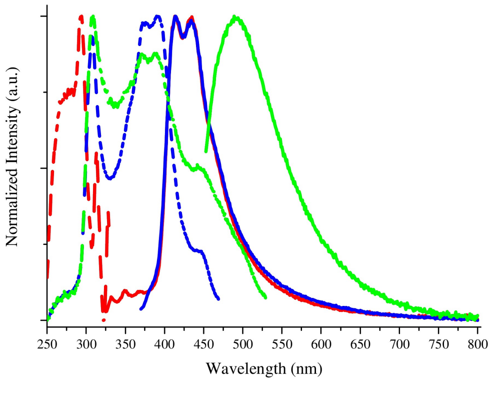

Figure 7. Normalized excitation (dotted lines) and emission (solid lines) spectra of **2Cl-film** at 298 K. Emission: $\lambda_{exc}=308$ nm (red), $\lambda_{exc}=350$ nm (blue) and $\lambda_{exc}=433$ nm (green). Excitation: $\lambda_{em}=350$ nm (red), $\lambda_{em}=491$ nm (blue) and $\lambda_{em}=550$ nm (green).

energy components are recognized as HEF and LEF (τ_{av} below instrumental resolution and 1.27 ns, respectively, see Figure S41), while the dominant emission reveals as HEP ($\tau_{av}=8.1$ ms, see Figure S42). MEP is greatly quenched with respect to crystalline **2Cl**, and appears as a broad, vibrationally unresolved emission only by its selective activation at 433 nm excitation. In fact, the presence of weak, unresolved absorption bands ($\tau_{av}=45$ ms, see Figure S43) in the 430–500 nm interval in the excitation spectrum of the film is observed. These absorptions are to be attributed to residual aggregated forms with a far less ordered supramolecular organization with respect to that of the crystalline sample and therefore indicated as S_0–T_D (D = dimers) in Table 1. The main peculiar feature of **2Cl** amorphous film is the intensity of HEP with respect to the other emissive components. It seems plausible that, in the crystalline phase, the T_1 state is easily depopulated in favour of triplet levels of the aggregates, T_H, resulting in more intense MEP than HEP. For amorphous **2Cl**, T_1–S_0 becomes the main phosphorescence deactivation channel. A similar behaviour, is indeed observed for crystalline **1Cl**, having a looser π-π interactions pattern. For what concerns HEF and LEF, it appears that HEF is weak regardless the crystalline grade of the sample, while LEF is apparently more intense in the crystalline phase. This observation could however be biased by the overlapping of LEF and HEP, therefore a clear comparison is difficult.

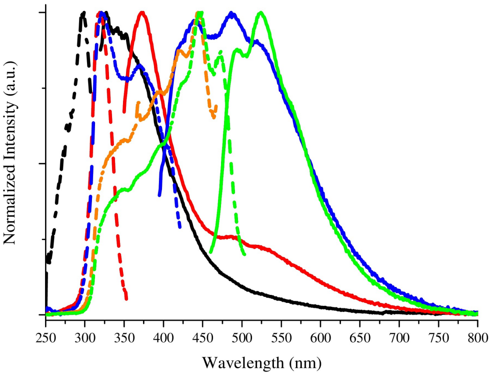

Figure 8. Normalized excitation (dotted lines) and emission (solid lines) spectra of **3Cl** crystals at 298 K. Emission: $\lambda_{exc}=300$ nm (black), $\lambda_{exc}=330$ nm (red), $\lambda_{exc}=374$ nm (blue) and $\lambda_{exc}=440$ nm (green). Excitation: $\lambda_{em}=327$ nm (black), $\lambda_{em}=373$ nm (red), $\lambda_{em}=441$ nm (blue), $\lambda_{em}=487$ nm (orange) and $\lambda_{em}=524$ nm (green).

Crystals of **3Cl** display as well excitation dependent emissive behaviour (see Figure 8 and Figure S46) with Φ in the 1–9% range (1% for $\lambda_{exc}=280$–310 nm; 7% for $\lambda_{exc}=320$–370 nm; 9% for $\lambda_{exc}=380$–450 nm) and multiple emission bands. In particular, when excited at 300 nm, a broad, partially resolved, emission is observed comprising a higher energy fluorescence,

Table 1. Photophysical parameters of **1–3Cl** at 298 and 77 K.

Sample		298 K					77 K				
	Φ (%)	λ_{exc} (nm)		λ_{em} (nm)		τ	λ_{exc} (nm)		λ_{em} (nm)		τ
1Cl	< 1 ($\lambda_{exc}=280$–300 nm)			333, 348	S_n–S_0	0.77 ns $^{c)}$	299	S_0–S_n	333, 349	S_n–S_0	1.22 ns$^{c)}$
	13 ($\lambda_{exc}=310$–340 nm)	313, 328	S_0–S_1	350	S_1–S_0	1.02 ns $^{c)}$	310, 327	S_0–S_1	367, 378, 383	S_1–S_0	4.76 ns$^{c)}$
	24 ($\lambda_{exc}=350$–390 nm)	367, 387	S_0–T_n	405, 428	T_1–S_0	269.74 μs $^{e)}$	368, 390	S_0–T_n	406, 429, 450	T_1–S_0	1.66 ms$^{e)}$
				510	T_H–S_0	25.99 ms $^{e)}$			487, 515	T_H–S_0	778.44 ms$^{e)}$
									558	T_σ–S_0	11.92 ms$^{a)}$
2Cl	< 1 ($\lambda_{exc}=280$–310 nm)	296	S_0–S_n	329	S_n–S_0	–$^{f)}$	298	S_0–S_n	329, 339, 348	S_n–S_0	–$^{f)}$
	6.3 ($\lambda_{exc}=320$–390 nm) 12 ($\lambda_{exc}=400$–460 nm)	327	S_0–S_1	397	S_1–S_0	1.41 ns $^{c)}$	310, 320, 325	S_0–S_1	362, 380, 401	S_1–S_0	1.48 ns$^{c)}$
		375, 399	S_0–T_n	434	T_1–S_0	1.33 ms $^{g)}$	376, 397	S_0–T_n	436	T_1–S_0	4.38 ms$^{d)}$
		439, 468	S_0–T_H	481, 512, 552	T_H–S_0	49.13 ms $^{d)}$	441, 469	S_0–T_H	483, 515, 554	T_H–S_0	530.56 ms$^{d)}$
									549	T_σ–S_0	12.68 ms$^{b)}$
2Cl-film	1 ($\lambda_{exc}=280$–310 nm) 3 ($\lambda_{exc}=320$–370 nm)	293	S_0–S_n	331, 349	S_n–S_0	– $^{f)}$					
	6 ($\lambda_{exc}=380$–410 nm)	310, 327	S_0–S_1	366, 382	S_1–S_0	1.27 ns $^{c)}$					
		372, 389	S_0–T_n	414, 434	T_1–S_0	8.09 ms $^{g)}$					
		430–500	S_0–T_D	491	T_D–S_0	45.11 ms $^{d)}$					
3Cl	1 ($\lambda_{exc}=280$–310 nm) 7 ($\lambda_{exc}=320$–370 nm)	298	S_0–S_n	327, 341, 349	S_n–S_0	–$^{f)}$	292, 298	S_0–S_n	318, 332	S_n–S_0	–$^{f)}$
	9 ($\lambda_{exc}=380$–450 nm)	320	S_0–S_1	373	S_1–S_0	0.65 ns $^{c)}$	314, 322, 331, 336	S_0–S_1	358, 380	S_1–S_0	0.96 ns $^{c)}$
		370, 406	S_0–T_n	416, 438	T_1–S_0	13.66 ms $^{d)}$	347–406	S_0–T_n	416, 439	T_1–S_0	516.60 ms$^{d)}$
		445, 474	S_0–T_H	492, 523	T_H–S_0	142.45 ms $^{d)}$	421, 447, 474	S_0–T_H	490, 521	T_H–S_0	700.58 ms$^{d)}$
									550	T_σ–S_0	11.22 ms$^{b)}$

[a)] $\lambda_{exc}=260$ nm; [b)] $\lambda_{exc}=280$ nm; [c)] $\lambda_{exc}=300$ nm; [d)] $\lambda_{exc}=320$ nm; [e)] $\lambda_{exc}=330$ nm; [f)] below instrumental resolution: 6 ps; [g)] $\lambda_{exc}=370$ nm.

HEF, centered at about 340 nm (lifetime shorter than the instrumental resolution: 6 ps) and a lower energy one, LEF, at about 370 nm ($\tau_{av}=0.65$ ns, see Figure S48), better resolved by exciting at 330 nm. In addition, a high energy phosphorescence, HEP, centered at about 438 nm ($\tau_{av}=13.7$ ms, see Figure S49) is selectively observed by exciting at 374 nm. Finally, MEP appears as a resolved band with vibronic replicas at 492 and 523 nm ($\tau_{av}=142.4$ ms, see Figure S50) by exciting at 440 nm.

At 77 K, by exciting at high energy, 280 nm, as previously observed for the other halo-derivatives of the **TT**-family, the broad low energy phosphorescence, LEP, centered at 552 nm ($\tau_{av}=11.2$ ms, see Figure S56) is activated together with a high energy emission centered at about 370 nm (see Figure 9 and Figure S51). This latter is the result of the convolution of HEF and LEF (τ_{av} below instrumental resolution and 0.96 ns, respectively, see Figure S53) with partially resolved vibrational peaks at 318 and 332 nm and 358 and 380 nm, respectively, as revealed by excitation at 330 nm, where LEF is better resolved. By 373 nm excitation, HEP (at about 416 and 439 nm; $\tau_{av}=516.6$ ms, see Figure S54) is activated together with MEP ($\tau_{av}=700.6$ ms, see Figure S55). This latter, better resolved by exciting at 440 nm, is identified by the presence of structured band with replicas at 490 and 521 nm.

Analysis of excitation profiles (see Figure 8, Figure 9, Figure S47 and Figure S52), reveals the presence of a narrow absorption at 298 nm, reasonably corresponding to S_n; an additional band at about 320 nm better vibrationally resolved at 77 K (replicas at 314, 322, 331 and 336 nm) to be assigned to S_1; one component at 370 and 406 nm, associated with molecular triplet levels including T_1 and a low energy structured band with peaks at 421, 447 and 474 nm. This latter, to be assigned to tightly bounded π-π aggregates as in **2Cl**.

The results obtained for the three compounds can be summarized as follow. They all display: dual fluorescence from S_1 and S_n, LEF and HEF respectively, when excited at high energy; a high energy phosphorescence, HEP, to be correlated to a molecular triplet level of π-π* character, T_1, only slightly distorted with respect to the ground state geometry as suggested by the small excitation-emission Stokes shift; an aggregation induced MEP which intensity increases by increasing the crystalline grade of the samples and the strength of π-π interactions in the crystal structure (intensity increasing in the order: **2Cl** amorphous film $<$ **1Cl** crystals $<$ **3Cl**$\cong$**2Cl** crystals). MEP and HEP appear to be competitive deactivation channels as evidenced by comparing crystals and the amorphous phase of **2Cl**. Finally, all the three compounds show at 77 K only a LEP emission whose origin is associated with the presence of high energy triplets of π-σ* character T_σ, see below, accessible from close π-π* singlets. The high Stokes shift of LEP suggests a highly distorted geometry of the excited state.

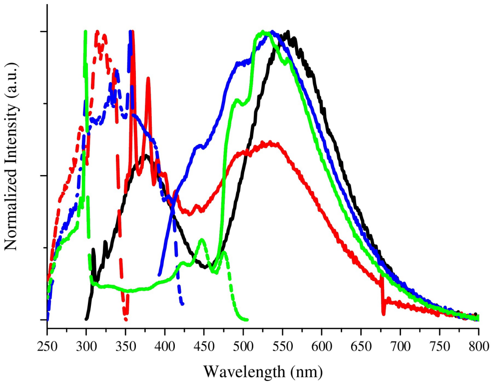

Figure 9. Normalized excitation (dotted lines) and emission (solid lines) spectra of **3Cl** crystals at 77 K. Emission: $\lambda_{exc}=280$ nm (black), $\lambda_{exc}=330$ nm (red), $\lambda_{exc}=373$ nm (blue) and $\lambda_{exc}=440$ nm (green). Excitation: $\lambda_{em}=373$ nm (red), $\lambda_{em}=443$ nm (blue) and $\lambda_{em}=526$ nm (green).

Interpretation of the origin of the different emission contributions of **1**–**3Cl** is based, as far as the supramolecular MEP is concerned, on its similarity with ultralong phosphorescence reported in previous studies on π-π aggregates of **TT** derivatives[6,7,12–15] and other compounds.[5] On the other hand, in the attempt to gain more information regarding the photophysical behaviour of the three compounds at molecular level, blended films of **1**–**3Cl** in polymethylmetacrilate, PMMA, 0.5 wt% have been prepared and analysed at 298 K. Unfortunately, as it occurs in diluted solution, a detailed investigation is difficult due to negligible quantum efficiency ($\Phi < 1\%$) of such dispersed systems and the possible presence of artifacts associated with the low signals. It has however to be noted that the three films display similar emissive behaviour (see Figure S26, Figure S44 and Figure S57), comprising HEF, LEF, HEP and MEP. The appearance of MEP is not surprising because, even at low chromophore loading, the formation of small aggregates cannot be avoided, in the same way as observed for diluted solutions. In addition, the presence of HEP for the films may be justified by partial protection from oxygen quenching by the PMMA matrix.

Interpretation of the electronic behaviour at molecular level is efficaciously obtained by DFT/TDDFT calculations performed on isolated 'gas-phase' compounds. Calculations nicely reproduce the fine structure of the high energy excitation spectra (see Figure S58 for the simulated spectrum, Figure 10 for a schematic representation of the electronic levels, Figures S59–S61 for the plots of the frontier molecular orbitals and Tables S3–S5 for full details of the computed transitions). Such agreement suggests that these states are of molecular origin freed from aggregation phenomena. Analysis of the electronic levels computed for the three compounds shows that: *i*) the calculated S_1 state, having (π,π*) character, corresponds to the excitation peak at about 330 nm responsible for LEF. Its oscillator strength is low ($f=0.013$ and 0.009 in **1Cl** and **2Cl**, respectively) or even zero (in **3Cl**) due to symmetry reasons, explaining why it is not detectable in the absorption spectrum (see Figures S12, Figure S27 and Figure S45); *ii*) the first (π,π*) singlet levels having large oscillator strength (S_3 and S_4, $f > 0.4$, see Figure 10) correspond to the peak below 300 nm observed in both the absorption and excitation spectra, responsible for HEF. The large energy gap between these states and S_1 could be the reason of the observed dual fluorescence; *iii*) all triplet levels below S_1 have the same (π,π*) character of S_1, in agreement with reduced distortion of the lower energy triplet state, T_1; *iv*) in **1Cl** and **2Cl**, the presence of a triplet level (T_8) of

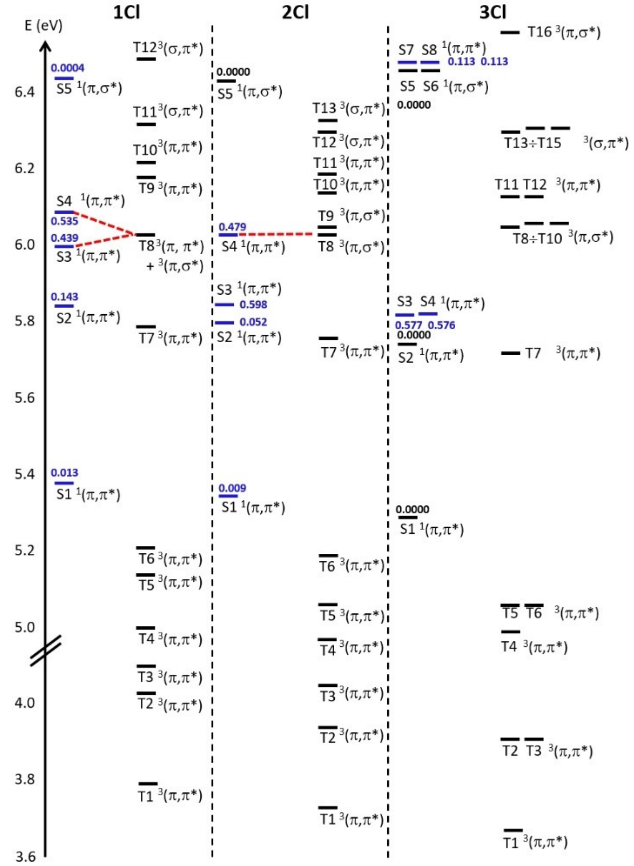

Figure 10. Scheme of singlet and triplet electronic levels with oscillator strengths (only for singlet states, in blue) and character for **1Cl** (left), **2Cl** (centre) and **3Cl** (right) at ωB97X/6-311++G(d,p) level of theory.

partial or full (for **1Cl** or **2Cl**, respectively) (π,σ*) symmetry close to S_4 could explain the unstructured LEP which, in fact, is only produced by high energy (260-280 nm) excitation. Based on El Sayed rules, the different symmetry of S_4 and T_8 guarantees an efficient singlet-to-triplet (S–T) intersystem crossing (ISC), further facilitated by the presence of the 'heavy' chlorine atom. In **3Cl**, having isoenergetic S_3 and S_4 levels rather below isoenergetic T_8–T_{10} levels, such S–T ISC process seems apparently forbidden for energetic reasons (see Figure 10). However, it should be noted that, in solid state, packing forces lead to symmetry breaking of **3Cl** from the ideal C_{3h} one displayed in the simulated gas-phase. Comparison with non-symmetrical **1Cl** and **2Cl**, having both S_3, S_4 and T_8–T_{10} levels well separated, suggests that for **3Cl** in crystal phase these levels are split as well, implying that S_4 and T_8 get closer enabling S–T ISC. In all the three compounds, emission from the relaxed T_8 state is expected to correspond to highly distorted geometry, owing to the σ contribution to the transition, explaining its observation at much lower energy than T_1.

Conclusion

The synthesis, characterization and photophysical behaviour of the mono-, di- and trichloro-**TT** compounds are here reported. The unravelling of the intricated emissive features is achieved through theoretical DFT/TDDFT calculations, crystal structure analysis and comparison with previous halo-derivatives of **TT.** **1**–**3Cl** are hardly emissive in solution but good emitters in the solid state due to an extended network of intermolecular interactions which activate multiple radiative deactivation channels comprising fast and long lived components. As for previous congeners, dual fluorescence and low energy phosphorescence from T_σ level are observed. One peculiar feature of **1**–**3Cl** is the competition between HEP and MEP, the latter prevailing in crystals of **2**–**3Cl** characterized by stronger π-π interactions. Moreover, AIE features are more effective (solid state higher quantum efficiency) in **1**–**3Cl** with respect to Br and I **TT**-derivatives. This observation can be explained by the lower heavy-atom effect played by chlorine leading to a less efficient $T_{1/H}$–S_0 ISC.

This study provides further insight in the photophysics of **TT**-based luminophores, confirming **TT** as a useful scaffold for the design of efficient RTP emissive materials for sensors, data security and bioimaging applications.

Experimental Section

General information. All reagents and model molecules were purchased from chemical suppliers and used without further purification unless otherwise stated. Triimidazo[1,2-*a*:1′,2′-*c*:1′′,2′′-*e*][1,3,5]triazine (**TT**) was prepared according to literature procedures.[16] All solvents used for HPLC analysis were of LC-MS grade. Thin layer chromatography (TLC) was performed using Merck silica gel 60 F254 precoated plates. Column chromatography was carried out with Biotage™ apparatus equipped with silica gel columns. Melting points were determined with a capillary melting point apparatus Stuart Scientific SMP3. Infrared spectra were collected in ATR mode on a Biorad FTS-60 A spectrometer. Elemental analyses were carried out at the Microanalytical Laboratory of the University of Milan with a PerkinElmer 2400 instrument. ^{1}H and ^{13}C NMR spectra were recorded at 300 K on a Bruker AVANCE-400 instrument (400 MHz) equipped with a BBI 1H/Multinuclear Probe Chemical, shifts are reported in parts per million (ppm) and are referenced to the residual solvent peak (DMSO, ^{1}H: $\delta = 2.50$ ppm, ^{13}C: $\delta = 39.50$ ppm). Coupling constants (J) are given in hertz (Hz) and are quoted to the nearest 0.5 Hz. Peak multiplicities are described in the following way: s, singlet; d, doublet. Mass spectra were recorded on a Thermo Fisher LCQ Fleet Ion Trap Mass Spectrometer equipped with UltiMate™ 3000 high-performance liquid chromatography (HPLC) system. HRMS spectra were obtained using Synapt G2-Si QTof mass spectrometer (Waters) with ZsprayTM ESI-probe for electrospray ionization (Waters) UV-Visible spectra were collected by a Shimadzu UV3600 spectrophotometer. Absolute photoluminescence quantum yields were measured using a C11347 (Hamamatsu Photonics K.K). A description of the experimental setup and measurement method can be found in the article of K. Suzuki et al.[17] For any fixed excitation wavelength, the fluorescence quantum yield Φ is given by:

$$\Phi = \frac{\mathrm{PN(Em)}}{\mathrm{PN(Abs)}} = \frac{\int \frac{\lambda}{hc}\left[I_{em}^{sample}(\lambda) - I_{em}^{reference}(\lambda)\right] d\lambda}{\int \frac{\lambda}{hc}\left[I_{ex}^{reference}(\lambda) - I_{ex}^{sample}(\lambda)\right] d\lambda}$$

where PN(Em) is the number of photons emitted from a sample and PN(Abs) is the number of photons absorbed by a sample, λ is the wavelength, h is Planck's constant, c is the velocity of light, $I_{em}^{sample}(\lambda)$ and $I_{em}^{reference}(\lambda)$ are the photoluminescence intensities with and without a sample, respectively, $I_{ex}^{sample}(\lambda)$ and $I_{ex}^{reference}(\lambda)$ are the integrated intensities of the excitation light with and without a sample, respectively. PN(Em) is calculated in the wavelength interval [λ_i, λ_f], where λ_i is taken 10 nm below the excitation wavelength, while λ_f is the upper end wavelength in the emission spectrum. Steady state emission and excitation spectra and photoluminescence lifetimes were obtained using both a FLS 980 (Edinburgh Instrument Ltd) and a Nanolog (Horiba Scientific) spectrofluorimeter composed of a iH320 spectrograph equipped with a Synapse QExtra charge-coupled device. The steady state measurements were recorded by excitation with a monochromated 450 W Xenon arc lamp and the spectra are corrected for the instrument response. Photoluminescence lifetime measurements were performed using Edinburgh Picosecond Pulsed Diode Laser EPL-375, EPLED-300, (Edinburgh Instruments Ltd) and microsecond flash Xe-lamp (60 W, 0.1 ÷ 100 Hz) with data acquisition devices time correlated single-photon counting (TCSPC) and multi-channel scaling (MCS) methods, respectively. Nanolog TCSPC measurements were performed using DeltaTime series DD-300 DeltaDiode and a DD-405 L DeltaDiode Laser, with a PPD-850 single photon detector module and are analysed with the instrument software DAS6. Average lifetimes are obtained as $\tau_{av} = \sum \frac{A_i \tau_i^2}{A_i \tau_i}$ from bi-exponential or three-exponential fits. Low temperature measurements are performed in a quartz dewar by immersion of the sample in liquid nitrogen or with a variable temperature liquid nitrogen cryostat Oxford DN1704. Films of **1–3Cl** dispersed in polymethylmethacrylate (PMMA) were prepared by spin coating (2000 rpm, 60 s) few drops of a DCM solution (**1-3Cl**/PMMA = 0.5 wt%; PMMA = 10 wt% with respect to the solvent) on a quartz substrate.

Synthetic Procedures and Characterization Data

General procedure for the synthesis of 3-chlorotriimidazo[1,2-a:1′,2′-c:1″,2″-e][1,3,5]triazine (**1Cl**), 3,7-dichlorotriimidazo[1,2-a:1′,2′-c:1″,2″-e][1,3,5]triazine (**2Cl**) and 3,7,11-trichlorotriimidazo[1,2-a:1′,2′-c:1″,2″-e][1,3,5]triazine (**3Cl**).

Compounds **1–3Cl** were prepared by chlorination of cyclic triimidazole **TT** with *N*-chlorosuccinimide (NCS) and catalytic trifluoroacetic acid (TFA) in acetonitrile. In a typical reaction, in a one-necked flask with a magnetic stirrer 500 mg (2.52 mmol) of **TT** were dissolved in CH_3CN (150 mL) at room temperature and few drops of TFA were added to the solution. A solution of NCS in CH_3CN (10 mg/mL) was then slowly added through a dropping funnel in 30 minutes (*case a*: 2 eq. of NCS, *case b*: 4 eq. of NCS). The reaction was stirred for 16 hours giving a mixture of **1Cl**, **2Cl** and **3Cl**, as revealed by thin layer chromatography (CH_2Cl_2:CH_3CN = 8 : 2; for **1Cl** R_f = 0.30; for **2Cl** R_f = 0.60; for **3Cl** R_f = 0.84). The reaction mixture was then added with 20 mL of acetone and the solvent was evaporated to dryness. The crude product was purified by Biotage supported column chromatography on SiO_2 with gradient elution. Gradient from CH_2Cl_2 = 100 to CH_2Cl_2 : CH_3CN = 30 : 70; Case a (2 eq): yield of **1Cl** = 47%; yield of **2Cl** = 38%; yield of **3Cl** = 3%. Case b (4 eq): yield of **1Cl** = 21%; yield of **2Cl** = 61%; yield of **3Cl** = 16%.

3-chlorotriimidazo[1,2-a:1′,2′-c:1″,2″-e][1,3,5]triazine (1Cl) **NMR data (9.4 T, DMSO-d6, 298 K, δ, ppm): ^{1}H NMR** 7.99 (1H, d, *J* = 1.7 Hz), 7.94 (1H, d, *J* = 1.7 Hz), 7.35 (1H, s), 7.32 (1H, d, *J* = 1.7 Hz), 7.28 (1H, d, *J* = 1.7 Hz); **^{13}C NMR** 135.6, 135.0, 134.9, 128.3 (*C*H), 128.2 (*C*H), 125.3 (*C*H), 111.4 (*C*H), 111.3 (*C*H), 111.0 (*C*Cl). **HRMS** (ESI-positive ion mode): calcd for $C_9H_6ClN_6$ 233.0342 $[M+H]^+$, found 233.0342. **FTIR-ATR** ν (cm^{-1}): 3090, 1610, 1582, 1512, 1454, 1425, 1327, 1242, 1161, 1132, 1109, 966, 906, 860, 812, 764, 725, 685. **Elemental Analysis** Anal. Calcd. for $C_9H_5ClN_6$ (%): C, 46.47; H, 2.17; N, 36.13. Found: C, 46.50; H, 2.27; N, 35.01. **Melting point** 215 °C.

3,7-dichlorotriimidazo[1,2-a:1′,2′-c:1″,2″-e][1,3,5]triazine (2Cl) **NMR data (9.4 T, DMSO-d6, 298 K, δ, ppm): ^{1}H NMR** 7.99 (1H, d, *J* = 1.7 Hz), 7.39 (1H, s), 7.35 (1H, s), 7.32 (1H, d, *J* = 1.7 Hz); **^{13}C NMR** 135.0, 134.9, 134.4, 128.4 (*C*H), 125.5 (*C*H), 125.3 (*C*H), 111.3 (*C*Cl), 111.2 (*C*H), 111.1 (*C*Cl). **HRMS** (ESI-positive ion mode): calcd for $C_9H_5Cl_2N_6$ 266.9953 $[M+H]^+$, found 266.9955. **FTIR-ATR** ν (cm^{-1}): 3123, 3086, 1582, 1510, 1429, 1315, 1238, 1175, 1146, 1130, 1097, 1070, 995, 932, 904, 878, 829, 748, 685. **Elemental Analysis** Anal. Calcd. for $C_9H_4Cl_2N_6$ (%): C, 40.48; H, 1.51; N, 31.47. Found: C, 41.17; H, 1.59; N, 31.29. **Melting point** 256 °C.

3,7,11-trichlorotriimidazo[1,2-a:1′,2′-c:1″,2″-e][1,3,5]triazine (3Cl) **NMR data (9.4 T, DMSO-d6, 298 K, δ, ppm): ^{1}H NMR** 7.40 (1H, s); **^{13}C NMR** 135.4, 125.6 (*C*H), 111.4 (*C*Cl). **HRMS** (ESI-positive ion mode): calcd for $C_9H_4Cl_3N_6$ 300.9563 $[M+H]^+$, found 300.9561. **FTIR-ATR** ν(cm^{-1}): 3092, 1587, 1514, 1429, 1302, 1230, 1171, 1101, 930, 870, 812, 679. **Elemental Analysis** $C_9H_3Cl_3N_6$ (%): C, 35.85; H, 1.00; N, 27.87. Found: C, 36.25; H, 1.07; N, 27.53. **Melting point** 266 °C.

Crystal Structure Analysis

Single-crystal X-ray diffraction data for compounds **1Cl**, **2Cl** and **3Cl** were collected on a Bruker APEX II CCD area detector diffractometer, using graphite-monochromated Mo Kα radiation (λ = 0.71073 Å). Data collections for all compounds were performed at room temperature. A full sphere of reciprocal space was scanned by 0.5° ω step, collecting 2160 frames in six different regions of the reciprocal space. After integration, an empirical absorption correction was made on the basis of the symmetry-equivalent reflection intensities measured.[18,19] The structures were solved by direct methods[20] and subsequent Fourier synthesis; they were refined by full-matrix least-squares on F^2 (SHELX 2014[21]) using all reflections. Weights were assigned to individual observations according to the formula $w = 1/[\sigma^2(F_o^2) + (aP)^2 + bP]$, where $P = (F_o^2 + 2F_c^2)/3$; a and b were chosen to give a flat analysis of variance in terms of F_o^2. Anisotropic parameters were assigned to all non-hydrogen atoms. All the hydrogen atoms were placed in idealized position and refined riding on their parent atom with an isotropic displacement parameter 1.2 times that of the pertinent parent atom. Crystal data, data collection and refinement details of the structural analyses are summarized in Table S2.

Computational details

Computational studies have been performed on gas-phase isolated **1Cl**, **2Cl** and **3Cl** using the Gaussian 16 suite of programs[22] at the ωB97X/6-311++G(d,p) level of theory. The ωB97X functional[23] has been chosen in view of its optimal performance in treating the geometrical and electronic features of **TT** derivatives,[6,7,12,14,15] including π-π interactions that play an important role in the photophysics of the present structures. In particular, it was previously verified[6] that other largely used functionals such as PBE0 are not able to provide stable π-π stacked dimeric units of **TT**.

Deposition Numbers 2051883 (for **1Cl**), 2051884 (for **2Cl**), and 2051885 (for **3Cl**) contain the supplementary crystallographic data for this paper. These data are provided free of charge by the joint

Cambridge Crystallographic Data Centre and Fachinformationszentrum Karlsruhe Access Structures service www.ccdc.cam.ac.uk/structures.

Acknowledgements

The use of instrumentation purchased through the Regione Lombardia-Fondazione Cariplo joint SmartMatLab Project is gratefully acknowledged.

Conflict of Interest

The authors declare no conflict of interest.

Keywords: Aggregation induced emission · DFT and TDDFT calculations · Mild chlorination · Organic materials · Phosphorescence

[1] W. Qin, P. Zhang, H. Li, J. W. Y. Lam, Y. Cai, R. T. K. Kwok, J. Qian, W. Zheng, B. Z. Tang, *Chem. Sci.* **2018**, *9*, 2705–2710.
[2] L. Gu, H. Wu, H. Ma, W. Ye, W. Jia, H. Wang, H. Chen, N. Zhang, D. Wang, C. Qian, Z. An, W. Huang, Y. Zhao, *Nat. Commun.* **2020**, *11*, 944.
[3] R. Gao, D. Yan, *Chem. Commun.* **2017**, *53*, 5408–5411.
[4] S. Hirata, K. Totani, J. Zhang, T. Yamashita, H. Kaji, S. R. Marder, T. Watanabe, C. Adachi, *Adv. Funct. Mater.* **2013**, *23*, 3386–3397.
[5] Z. An, C. Zheng, Y. Tao, R. Chen, H. Shi, T. Chen, Z. Wang, H. Li, R. Deng, X. Liu, W. Huang, *Nat. Mater.* **2015**, *14*, 685–690.
[6] E. Lucenti, A. Forni, C. Botta, L. Carlucci, C. Giannini, D. Marinotto, A. Previtali, S. Righetto, E. Cariati, *J. Phys. Chem. Lett.* **2017**, *8*, 1894–1898.
[7] E. Lucenti, A. Forni, C. Botta, L. Carlucci, C. Giannini, D. Marinotto, A. Pavanello, A. Previtali, S. Righetto, E. Cariati, *Angew. Chem. Int. Ed.* **2017**, *56*, 16302–16307; *Angew. Chem.* **2017**, *129*, 16520–16525.
[8] R. Kabe, C. Adachi, *Nature* **2017**, *550*, 384–387.
[9] O. Bolton, K. Lee, H.-J. Kim, K. Y. Lin, J. Kim, *Nat. Chem.* **2011**, *3*, 205–210.
[10] H. Shi, Z. An, P.-Z. Li, J. Yin, G. Xing, T. He, H. Chen, J. Wang, H. Sun, W. Huang, Y. Zhao, *Cryst. Growth Des.* **2016**, *16*, 808–813.
[11] Z. Lin, R. Kabe, N. Nishimura, K. Jinnai, C. Adachi, *Adv. Mater.* **2018**, *30*, 1803713.
[12] E. Lucenti, A. Forni, C. Botta, L. Carlucci, A. Colombo, C. Giannini, D. Marinotto, A. Previtali, S. Righetto, E. Cariati, *ChemPhotoChem* **2018**, *2*, 801–805.
[13] E. Lucenti, A. Forni, C. Botta, C. Giannini, D. Malpicci, D. Marinotto, A. Previtali, S. Righetto, E. Cariati, *Chem. Eur. J.* **2019**, *25*, 2452–2456.
[14] A. Previtali, E. Lucenti, A. Forni, L. Mauri, C. Botta, C. Giannini, D. Malpicci, D. Marinotto, S. Righetto, E. Cariati, *Molecules* **2019**, *24*, 2552.
[15] E. Lucenti, A. Forni, A. Previtali, D. Marinotto, D. Malpicci, S. Righetto, C. Giannini, T. Virgili, P. Kabacinski, L. Ganzer, U. Giovanella, C. Botta, E. Cariati, *Chem. Sci.* **2020**, *11*, 7599–7608.
[16] D. M. Schubert, D. T. Natan, D. C. Wilson, K. I. Hardcastle, *Cryst. Growth Des.* **2011**, *11*, 843–850.
[17] K. Suzuki, A. Kobayashi, S. Kaneko, K. Takehira, T. Yoshihara, H. Ishida, Y. Shiina, S. Oishic, S. Tobita, *Phys. Chem. Chem. Phys.* **2009**, *11*, 9850–9860.
[18] G. M. Sheldrick, *SADABS*, Universität Göttingen, Germany **1996**.
[19] Bruker, *SADABS*, Bruker AXS Inc., Madison, Wisconsin, USA **n.d**.
[20] M. C. Burla, R. Caliandro, B. Carrozzini, G. L. Cascarano, C. Cuocci, C. Giacovazzo, M. Mallamo, A. Mazzone, G. Polidori, *J. Appl. Crystallogr.* **2015**, *48*, 306–309.
[21] G. M. Sheldrick, *Acta Crystallogr. Sect. C* **2015**, *71*, 3–8.
[22] M. J. Frisch, G. W. Trucks, H. B. Schlegel, G. E. Scuseria, M. A. Robb, J. R. Cheeseman, G. Scalmani, V. Barone, G. A. Petersson, H. Nakatsuji, X. Li, M. Caricato, A. V Marenich, J. Bloino, B. G. Janesko, R. Gomperts, B. Mennucci, H. P. Hratchian, J. V Ortiz, A. F. Izmaylov, J. L. Sonnenberg, Williams, F. Ding, F. Lipparini, F. Egidi, J. Goings, B. Peng, A. Petrone, T. Henderson, D. Ranasinghe, V. G. Zakrzewski, J. Gao, N. Rega, G. Zheng, W. Liang, M. Hada, M. Ehara, K. Toyota, R. Fukuda, J. Hasegawa, M. Ishida, T. Nakajima, Y. Honda, O. Kitao, H. Nakai, T. Vreven, K. Throssell, J. A. Montgomery Jr., J. E. Peralta, F. Ogliaro, M. J. Bearpark, J. J. Heyd, E. N. Brothers, K. N. Kudin, V. N. Staroverov, T. A. Keith, R. Kobayashi, J. Normand, K. Raghavachari, A. P. Rendell, J. C. Burant, S. S. Iyengar, J. Tomasi, M. Cossi, J. M. Millam, M. Klene, C. Adamo, R. Cammi, J. W. Ochterski, R. L. Martin, K. Morokuma, O. Farkas, J. B. Foresman, D. J. Fox, Gaussian 16, Revision A.03, Gaussian, Inc., Wallingford CT, **2016**.
[23] J.-D. Chai, M. Head-Gordon, *J. Chem. Phys.* **2008**, *128*, 084106.

Manuscript received: February 3, 2021
Revised manuscript received: March 12, 2021
Accepted manuscript online: March 16, 2021